Electrohydrodynamic phenomena in atmospheric discharges : application to airflow control by plasma actuators

Eric Moreau, Nicolas Benard
University of Poitiers,
Institut Pprime, CNRS-ISAE-ENSMA, France
e-mail: eric.moreau@univ-poitiers.fr

Abstract—**When a high potential difference is applied between at least two electrodes in atmospheric air, there is ionization of the air molecules around the active electrode. Due to the electric field, an electrohydrodynamic (or electrofluid-dynamic) force is produced, resulting in a flow called ionic or electric wind. This EFD phenomenon, that converts directly electrical energy into mechanical energy, has been widely studied for its many applications such as electrical blowers without fan, enhancement of heat transfer, plasma actuators for flow control and corona-based propulsion. In the first part of this paper, the last results on plasma actuators and their use for airflow separation control are presented. In a second part, future prospects offered by new plasma actuators such as µ-plasma grid for turbulence manipulation are discussed. Finally, recent experiments on DC corona discharges used as electrical blower and thruster are presented.**

I. INTRODUCTION

Corona discharges in atmospheric air have been widely studied for 15 years for their applications in aerodynamic flow control by plasma actuators. Even if the most used plasma actuator is based on a single surface dielectric barrier discharge (DBD) composed of two electrodes mounted on both sides of a dielectric, lots of others designs exist.

On one hand, if this surface DBD is supplied by a sine high voltage, an electrofluid-dynamic (EFD) force is produced and that results in an electric wind based-wall jet. Single DBD can produce mean force and electric wind velocity up to about 1 mN/W and 7 m/s, respectively. With multi-DBD designs, velocity up to 11 m/s has been measured and force up to 350 mN/m [1]. On the other hand, if the high voltage has a nanosecond repetitively pulsed waveform, the sudden gas heating at the dielectric wall results in a pressure wave with pressure gradient up to 10 kPa [2]. When the plasma actuator is mounted at the wall of an aerodynamic profile, these both mechanical phenomena (EFD force and pressure wave) can interact with the boundary layer and modify the near-wall flow, resulting in the control of the whole flow.

In this paper, the electrical, optical and mechanical characteristics of all these plasma actuators are presented and discussed. It is not possible to summarize all the studies concerning flow control by plasma actuators. Then we focus on one aerodynamic case: separation control along an airfoil. We will highlight the key role of the frequency actuation and the actuation location on the control effectiveness. Then, we will discuss about the future prospects offered by new plasma actuators such as µ-plasma grid for turbulence

manipulation [3]. Finally, recent experiments on the dynamic of the ionic wind produced by DC corona discharges used as thruster and blower are presented [4, 5].

II. Airflow Control by Plasma Actuators

A. Plasma Actuators

The most-used plasma actuator is the single DBD one based on two electrodes mounted on both sides of a dielectric. The air-exposed active electrode is connected to an ac high voltage power supply and the other one is grounded and encapsulated. Typically, geometrical parameters are as follows: electrode width of a few mm, electrode gap equal to zero or a few mm and a dielectric thickness from 50 µm to a few mm. The applied voltage ranges from a few kV up to 30 kV at a frequency equal to a few kHz. Figure 1 shows a top view of the electrode design and a photograph of a plasma actuator that is not supplied (two electrodes on both sides of a 2-mm thick glass plate). When the ac high voltage is applied, a surface plasma discharge is ignited, a illustrated by the photograph of Figure 2. More, the curves of voltage/current versus time and the iCCD visualisations of Figure 3 highlights that two discharges occur during one cycle. During the positive-going cycle, one can see long ionized channels that propagates along the dielectric wall; this is a positive streamer discharge. The negative-going cycle is associated to a negative glow discharge with some visible spots starting from the active electrode.

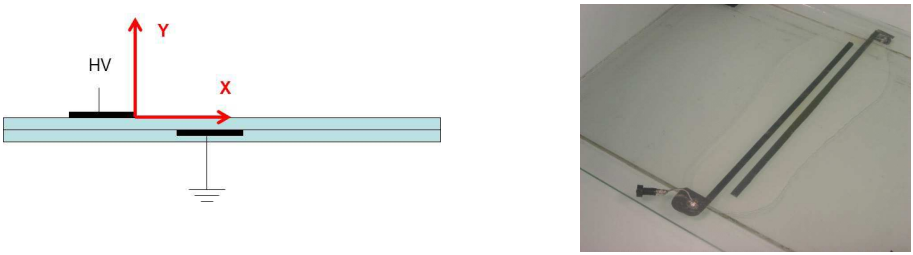

Fig. 1. Single DBD plasma actuator.

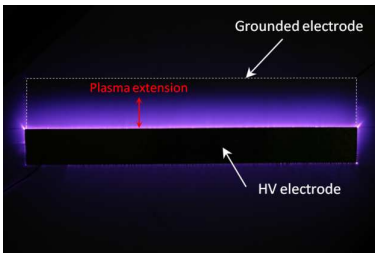

Fig. 2. Top-view of the surface discharge.

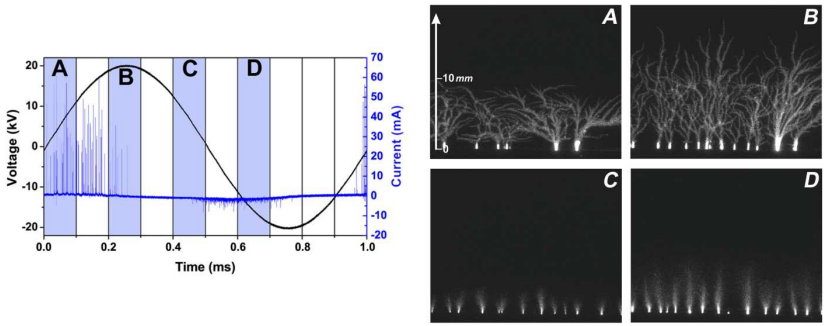

Fig. 3. Voltage and discharge current versus time (left) and top iCCD visualisations of the discharge in four different time windows (right).

In such conditions, a 2D linear wall jet is induced by the discharge, as illustrated by Figure 4 that shows the time-averaged velocity field measured by particle image velocimetry (PIV) above the dielectric wall where the discharge occurs. One can remark that the jet thickness is of a few mm and the maximum velocity is usually obtained at about 0.5 mm above the dielectric wall (maximum velocity of about 5.5 m/s in this case).

However, the produced electric wind is strongly unsteady and periodic. For instance, Figure 5 shows the velocity (at x = 5 mm and y = 1 mm, in red) versus time when a sine high voltage at 1 kHz (f_{AC}) is alternatively switched on and switched off at a burst frequency f_{BM} = 20 Hz with a duty cycle of 30 %. This measurement has been conducted with Laser Doppler Velocimetry (LDV) system. It highlights that two time scales coexist in the produced electric wind: the electric wind oscillations at the same frequency than the one of applied voltage at f_{AC} and larger amplitudes velocity fluctuations at f_{BM}. We will see later that this characteristics is very useful for flow control. Moreover, if the high voltage waveform at f_{AC} is modified, the temporal behaviour of the ionic wind velocity changes too. Results presented in Figure 6 clearly show that periods of U velocity production (horizontal velocity) correspond to the negative-going cycle of the applied HV. In contrast, the U velocity decreases during the streamer discharge occurring during the positive-going cycle of the voltage. It results that the U horizontal velocity component is a mirror of the input electrical waveform, with a phase-shift.

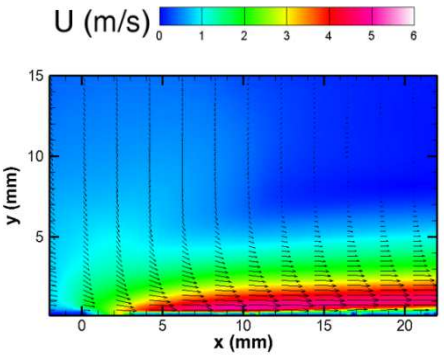

Fig. 4. Velocity field produced by a single DBD.

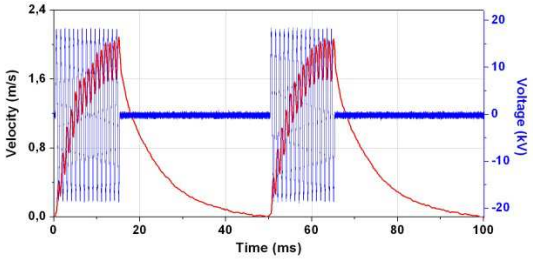

Fig. 5. Local velocity versus time.

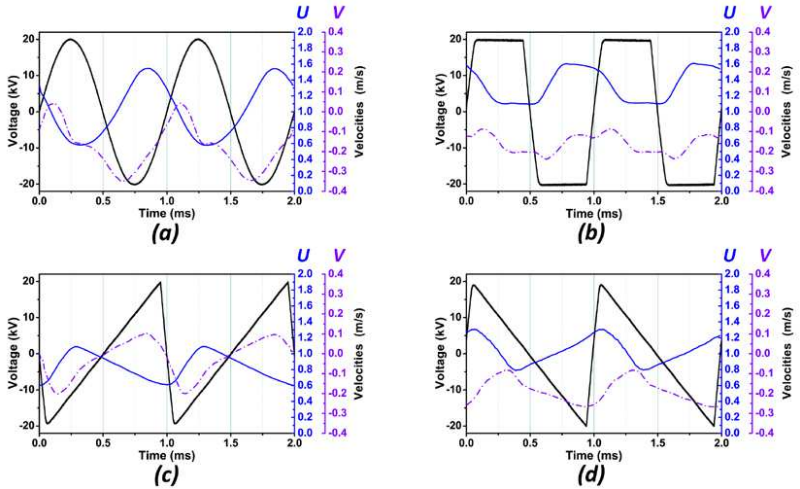

Fig. 6. time-resolved electric wind U (horizontal, *i.e.*, in the plasma layer direction) and V (normal direction) velocity for (a) a sine waveform input, (b) a square waveform, (c) a positive ramp voltage and (d) a negative ramp voltage. Location is x = 5 mm and y = 1 mm, V_{AC} = 18 kV and f_{AC} = 1000 Hz.

Another manner to characterize the mechanical effect of a plasma actuator is to measure with a laboratory balance the time-averaged thrust produced by the discharge, this thrust corresponding to the EFD force minus the skin-friction drag force due to ionic wind that flows along the dielectric wall (in practise, drag force is very small compared to EFD force). Figure 7 presents the thrust versus electrical power consumption in the case of a plate active air-exposed electrode and when this electrode is replaced by wires of different diameters. First, one can remark that thrust is a linear function of the electrical power consumption in this range, regardless of the electrode geometry. Secondly, the use of a thin wire active electrode instead of a plate one results in a higher thrust for a same electrical power consumption, suggesting an important increase in the actuator effectiveness. Finally, the best effectiveness is here equal to about 1 mN per consumed watt.

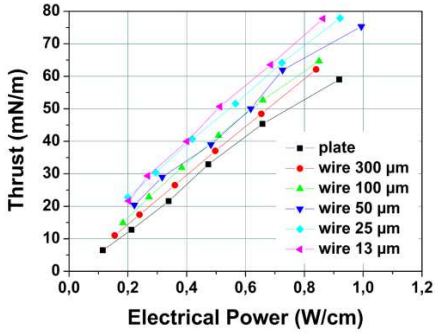

Fig. 7. Thrust versus electrical power (frequency = 1.5 kHz, voltages from 12 to 22 kV).

From this typical actuator design, lots of others actuator configurations have been developed such as multi-DBD actuators or sliding discharges. For instance, multi-DBD actuators consist of using several single DBD in series. Figure 8 shows an example of an original design for which two points have been optimized compared to usual multi-DBD. First, the plate air-exposed active electrodes have been replaced by thin wires (diameter of 25 µm) in order to enhance the electric wind produced by each single DBD. Secondly, interaction between successive DBD has been cancelled by alternating the HV electrode and the grounded one, from one DBD to the successive one. Figure 9 presents horizontal velocity profiles measured 0.6 mm above the wall, from x = 0 (position of the first wire HV electrode) to x = 145 mm (25 mm downstream the right edge of the last grounded electrode) for three different voltages, with the help of a home-made pressure sensor. From x = 0 to about 15 mm, the velocity increases from zero to 6 m/s for 24 kV and then decreases because there is no EFD force downstream the plasma extension. Then each successive single DBD add velocity that cumulates up to 10.5 m/s downstream the last single DBD, this in absence of a complete optimization of the actuator geometry.

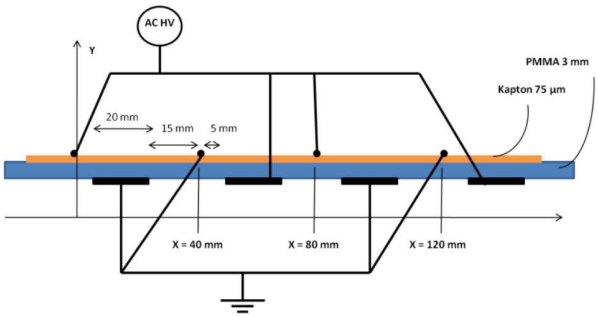

Fig. 8. Sketch of the multi-DBD plasma actuators composed of 4 successive single DBD.

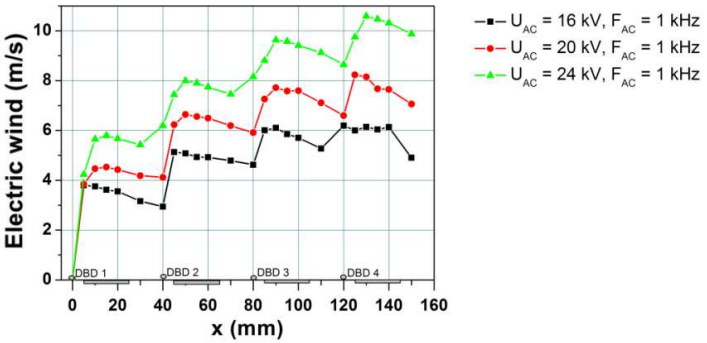

Fig. 9. Horizontal velocity profiles measured 0.6mm above an inversed multi-DBD actuator.

Finally, a new type of actuator supplied by a nanosecond pulsed high voltage has been widely investigated in the last years. In this case, the electrofluid-dynamic force is negligible and the major mechanical effect is the gas heating at the wall surface and the resulting pressure wave. The actuator (NS-DBD) is usually composed of two electrodes (1 and 2 in Figure 10) between which a pulsed voltage V_P is applied. In order to increase the area of the surface discharge, a third dc electrode (3) can be used; then a sliding discharge can be established (SL-DBD). Figure 11 presents voltage and current waveforms in the case of a NS-DBD. The current present two peaks (positive and negative), which appear respectively at the rising and decaying times of the voltage; the positive peak is caused by the propagation of charges within the plasma, from the electrode edge (1) to the dielectric surface. With voltage and current data, instantaneous power is computed, revealing that the power consumed by the actuator is about a tens of kW/cm during a time laps less than 20 ns (here, 18 kW/cm for V_P = 14 kV). However, the consumed energy per pulse is relatively weak (Fig. 11-D). Dissipated energy of 0.09 and 0.37 mJ/cm are observed for V_P = 10 and 18 kV, respectively.

Finally, Figure 12 shows top iCCD visualisations of a SL-DBD plasma actuator (Figure 10b) at a constant V_P = 14 kV and by increasing gradually the negative dc voltage (from 0 to -20 kV) at electrode (3). One can see that the dc voltage component starts to have an effect from V_{DC} = -12 kV. From -16 kV, the streamers produced by the nanosecond DBD propagate until electrode (3), inducing then a sliding discharge.

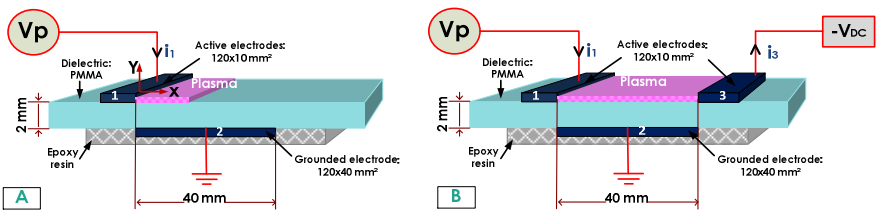

Fig. 10. Sketch of a typical nanosecond DBD plasma actuator

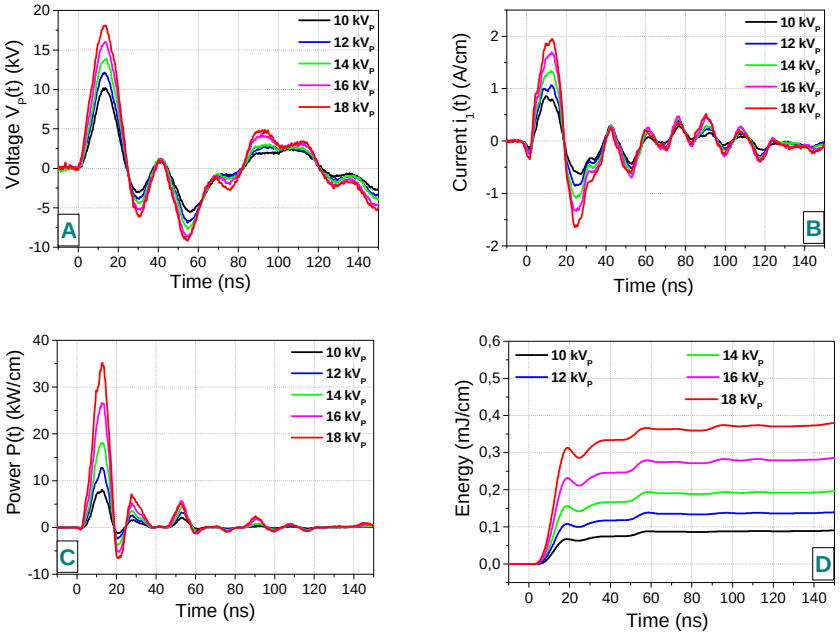

Fig. 11. Electrical diagnostics of the nanosecond NS-DBD: (A) pulsed voltage waveforms; (B) measured total currents $i_1(t)$; (C) total power and (D) energy released by pulse.

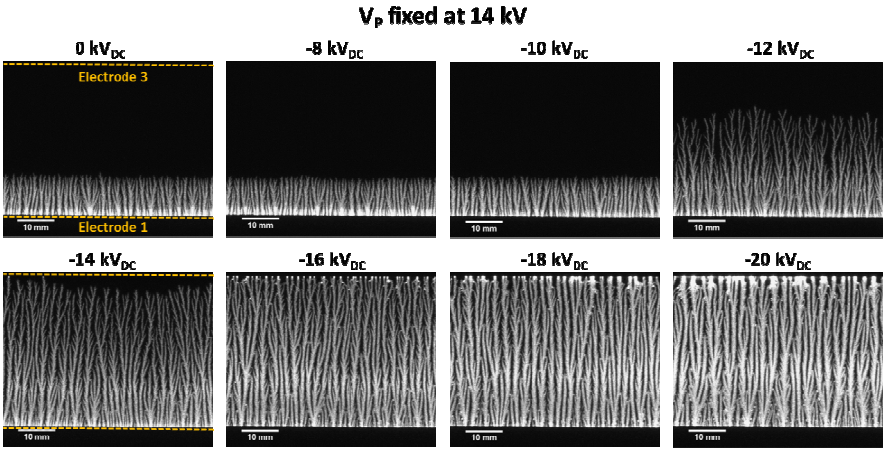

Fig. 12. ICCD top visualizations of the discharge with VP = 14 kV and several values of the dc voltage applied to electrode (3).

Figure 13a shows a Schlieren visualisation of the NS-DBD. At the dielectric wall, from the edge of the active electrode, one can see the thermal signature of the discharge. More, one can observe the hemispherical pressure wave that ignites at the electrode edge and

that propagates at sound velocity in the quiescent air. In Figure 13b, the value of the induced pressure versus energy per pulse is plotted. It highlights that this overpressure is proportional to the electrical energy and the slope of the curve is equal to about 2 kPa per mJ/cm.

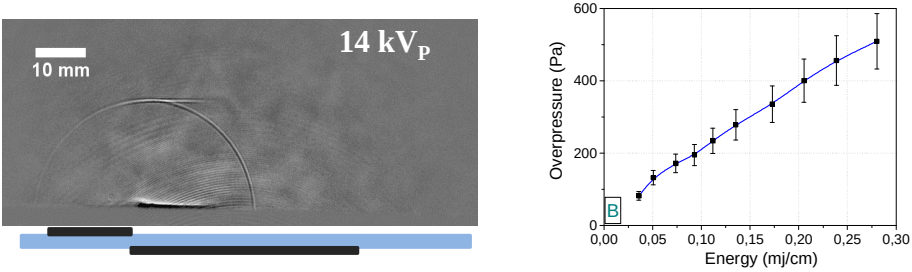

(a) (b)

Fig. 13. Schlieren visualisation the thermal and pressure effects of a NS-DBD (a) and pressure produced by a NS-DBD.

B. Airflow Control

For now a little bit more than 15 years, the ability of plasma actuators to manipulate airflow has been widely studied all over the world. It is not possible to summarize all these studies. In the present abstract, we focus on separation control along an airfoil. We will highlight the key role of the frequency actuation and the actuation location on the control effectiveness.

The goal of the first experimental study was to investigate the ability of surface AC-DBD plasma actuators to delay flow separation along the suction side of a NACA0015 airfoil. Three single surface DBD actuators that can operate separately are mounted on the suction side of the profile, at 18 %, 27 % and 37 % of the chord length. The boundary layer is transitioned by a tripper to be sure that the flow control is not due to the laminar-to-turbulent transition. The angle of attack is equal to 11.5° and the free-stream velocity to $U_0 = 40$ m/s, resulting in a chord-based Reynolds number of $Re_c = 1.33 \times 10^6$ (airfoil chord = 50 cm). The spanwise of the airfoil is equal to 120 cm and the electrode length to about 60 cm. Then the actuation occurs on 50 % of the airfoil spanwise. The flow is studied with a high-resolution PIV system. In such aerodynamic conditions, the baseline flow separation occurs at 50% of chord. Then, the different single DBD have been switched on separately, in order to investigate the actuator location effect. First, one highlighted that the DBD located at $x_c/c = 18$ % is more effective than the two others ones, with a separation delay up to 64% of chord. When the three DBDs operate simultaneously, the separation point moves progressively toward the trailing edge when the high voltage is increased, up to 76% of chord at 20 kV (Figures 14a).

Then, the operating frequency f_{AC} has been varied from 50 Hz up to 1 kHz, corresponding to a reduced frequency range of $0.31 < F^+_{ac} < 6.13$, this reduced frequency being estimated with the following relation: $F^+_{ac} = L_{sep} \times f_{AC} / U_0$ where L_{sep} is the separation length, *i.e.* 0.25 meter in our case. Figure 14b shows the separation point location as a function of the frequency actuation F^+_{ac} (V_{AC} set at 20 kV). From this plot, one can deduce that the most effective separation delay occurs for $F^+_{ac} = 3.1$, with a separation de-

layed to 80%. Knowing that the time-averaged electric wind velocity increases with f_{AC}, one could expect that the X_{sep} should have increased with f_{AC}. In practice, it is not the case. Indeed, at low frequency (F^+_{ac} = 0.31), the time-averaged velocity of the produced electric wind is weak (about 1.5 m/s). Subsequently, one can assume that the control authority is due to a frequency effect and not to a mean momentum effect. That is confirmed by the decrease of the effectiveness when F^+_{ac} is increased up to 0.93 for which the electric wind velocity is higher than the one at 0.31 (about 2.5 m/s). Finally, when F^+_{ac} is increased from 0.93 to 3.1, the time-averaged electric wind velocity increased up to about 4.5 m/s and one can think that the reattachment is mainly due to a momentum effect. At this stage, one cannot explain more precisely the frequency effect, because time-resolved near-wall measurements would be needed. Finally, Figure 15 presents an example of velocity field along the airfoil in the baseline case and when the flow is manipulated by plasma actuation. One can see that the delay of the separation point results in a strong reduction of the recirculation bubble downstream of the profile, which is usually at the origin of drag reduction and lift enhancement.

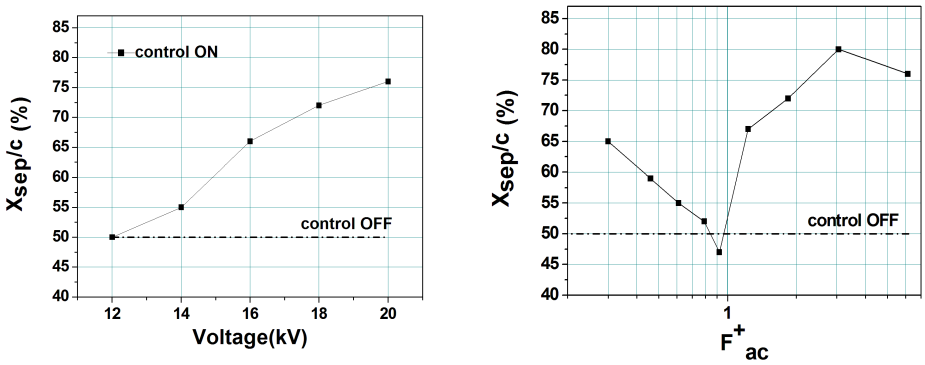

Fig. 14. Location of the separation point versus high voltage V_{AC} (a) and versus frequency f_{AC}.

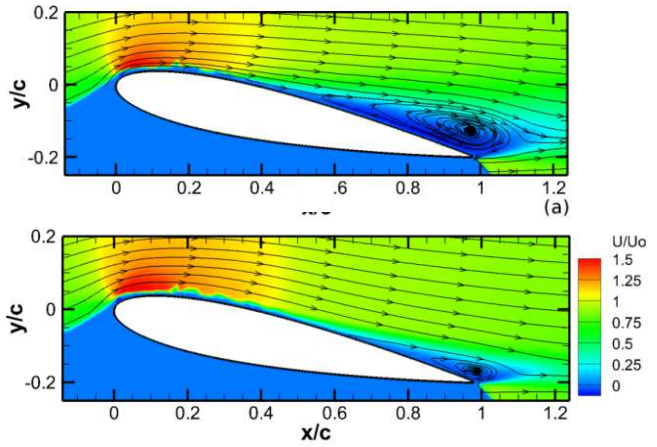

Fig. 15. Flow control by DBD (Re = 1.33×10^6) : visualisation of the flow by particle image velocimetry.

The goal of the second experimental study presented here is to investigate the ability of a surface nanosecond pulsed DBD (NS-DBD) plasma actuator, located at the leading edge of the airfoil, to delay flow separation along the suction side of the same NACA0015 airfoil inclined at 13.5 degrees. The free-stream velocity is still equal to $U_0 = 40$ m/s. With such conditions, the baseline flow separation occurs at about 50% of chord. One can remark that the flow separation is still at mid-chord since the angle of attack is higher than in the previous study. This is due to the fact that in the present study, there is no tripper at the leading edge of the airfoil because the actuator is located at the leading edge.

Two different actuation types have been used. First, the frequency F^+_{pulse} is varied from 0.26 to 10.6, corresponding to electrical power consumption from 8 mW/cm to 290 mW/cm. With such an actuation, the separation location moves progressively toward the trailing edge when the high voltage frequency F_{pulse} is increased (Figure 16, -■-). In the best case ($F^+_{pulse} = 10.6$, *i.e.* $F_{pulse} = 1630$ Hz), the separation point is delayed up to 85 %. This result shows that the actuation is more effective when the electrical power consumption increases, but no frequency effect can be really highlighted because one cannot separate the effect of the frequency with the one of the injected power. Secondly, the operating frequency F^+_{pulse} is set to a constant value and the pulsed high voltage is burst-modulated at a lower frequency F^+_{burst} with $0.1 \le F^+_{burst} \le 2.65$. With this actuation mode, the power injected in the flow is constant whatever F^+_{burst} (145 mW/cm); it is then possible to determine the frequency effect on the control authority. Indeed, in this case, the influence of the frequency is clearly observable and its effect on the separation point delay is not monotonous (Figure 16, -●-). On one hand, at $F^+_{burst} = 0.1$ and 2.65 (smallest and highest frequencies), the separation was delayed at about 60% of chord. On the other hand, in the frequency range $0.5 \le F^+_{burst} \le 0.8$, the flow separation occurred downstream of $x_c/c = 0.80$ with a most effective effect at $F^+_{burst} = 0.53$ with a delay of the separation location up to $x_c/c = 0.83$.

This study shows that NS-DBD plasma actuators can compete with others types of active control devices to reattach separated flow at high Reynolds number, with a very low power consumption (145 mW/cm, corresponding to a total consumption of 8.26 W for a 57-cm long electrode) and a weak induced pressure wave (300 Pa).

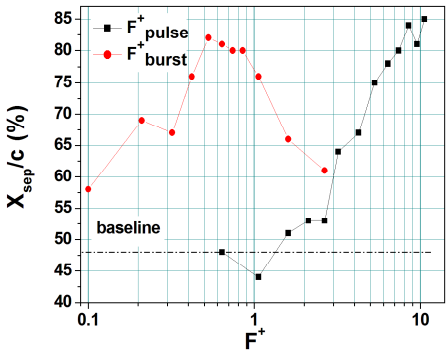

Fig. 16. Separation location versus frequency actuation in steady mode (■) and burst mode (●).

III. Others Applications

There are lots of others applications of the ionic wind produced by atmospheric discharges. In this part, we discuss only two applications. The first one deals with a new type of plasma actuators for turbulence control and combustion applications. The second one concerns the thrusters for near-space applications.

A. Plasma Grid for Mixing

This study interests in defining a new type of dielectric barrier discharge actuator for mixing improvement purpose [3]. Indeed, mixing of scalar flow component is important for a large number of practical and fundamental situations, such as combustion assisted by plasma. In practise, the plasma actuator is made of a ceramic plate (thickness of 1.27 mm) perforated by 121 holes having an inner diameter Φ of 2 mm (Figure 17). The top of the plasma actuator is made of a conductive layer (nickel with thickness of 10 µm) connected to a high voltage power supply. The grounded electrode is embedded within the ceramic dielectric material at a distance of 630 µm from the air-exposed electrode. The distance between the edge of an active electrode and the edge of the corresponding hole designed for the gas passage is 350 µm (Figure 17). The distance between the centres of two successive holes is 3.05 mm. At a sufficient onset voltage, the plasma discharge array is fully powered (see Figure 18), the electric field producing a visible discharge around each of the holes (at the surface, but also inside the lateral edge of the holes).

This honeycomb plasma discharge has been implemented at the exhaust of a circular open-air type wind-tunnel with a 0.132 m^2 cross-section. This facility has a 1.45 m long chamber, series of mesh grids and a jet exit of 50 mm in diameter is obtained by means of a contraction outlet which improves the flow uniformity. The local velocity (U_0), measured at the centre of one hole of the plasma actuator array, is fixed here to 10 m/s.

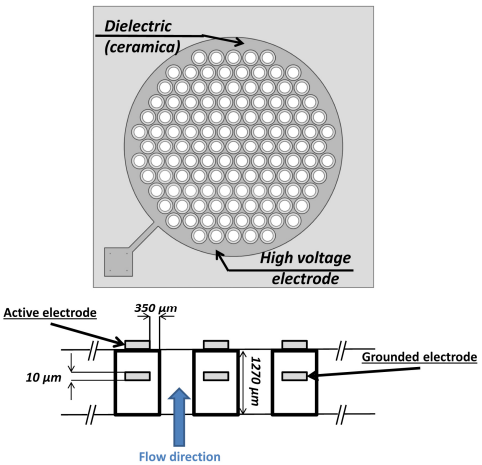

Fig. 17. Sketch (front and slice views) of the plasma actuator.

Fig. 18. Photographs of the plasma discharge array prototype (left), mounted at the jet exhaust (center) and powered by an AC voltage with peak amplitude of 7 kV_p at 2000 Hz.

Flow visualisations have been performed using a short-pulsed Nd:YLF laser synchronized with a fast camera (Photron SA-Z). Dielectric oil (Ondina 915) is atomized into fine droplets for permitting the laser light scattering. For each of the tests, a flow sequence of 5000 images has been recorded. The data processing on the raw images simply consists of removing the minimum of one acquisition sequence and computing the averaged grey level of the 5000 images. Images of the mean flow without plasma discharge for streamwise and cross-stream flow visualizations are presented in Figure 19, for U_0 = 10 m/s. The mean flow visualizations indicate that the multi-jet quickly evolves as a single jet with a potential core whose length can be easily estimated. Knowing that the use of burst modulation is an effective method for maximizing the amplitude of the imposed periodic perturbations, burst modulation actuation has been conducted for a sinusoidal waveform with voltage amplitude of 7 kV_p and f_{AC} frequency of 2000 Hz. The frequency f_{BM} imposed by the burst modulation ranges from 5 up to 400 Hz (St_D=0.018 to 1.49). The potential core length is estimated by grey level analysis of cross-stream visualisations, such as the right image of Figure 19. Figure 20 presents the potential core length versus actuation frequency (Strouhal number). More, a few visualizations of the mean flow are aloso introduced in Figure 20. This figure confirms that the thickness of the shear layer, its spreading rate and thus the length of the potential core are modified accordingly to the forcing frequency introduced by the burst modulation. For the worst cases, the length of the potential core remains similar to the one reported for the natural flow. However, a minima is found at St_D=0.37 with a reduction of 40%. One can assume that the reduction in the potential core is caused by a rapid growing of the annular shear layer and higher mixing rate is expected beyond the end of the potential core. These preliminary measurements are very promising and deeper studies are expected very soon.

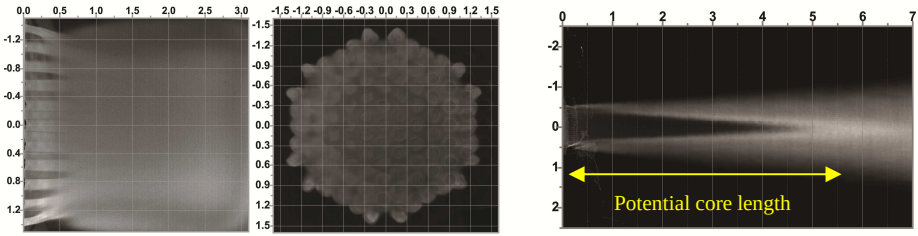

Fig. 19. Streamwise (including a zoomed view of the initial region) and cross-stream visualizations of the mean flow downstream of the multi-jet plasma device (the actuator is turned off).

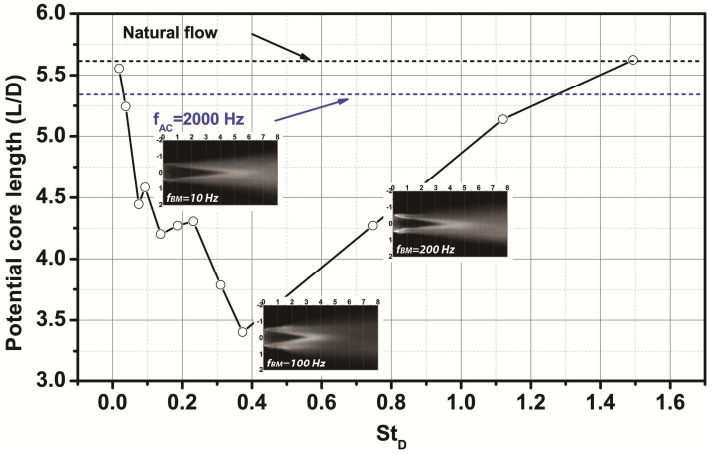

Fig. 20. Influence of Strouhal number of the actuation St_D on the length of the potential core.

B. DC Coronas and EHD Propulsion

In 1967, Christenson and Moller [6] published the first paper on EHD propulsion. They investigated theoretically and experimentally the capabilities of corona discharge to be used as thruster. In 2009, NASA published a report on ionic wind propulsion [7]. They concluded that if values of effectiveness equal to 20 N/kW (*i.e.* mN/W) and thrust per unit surface of 20 N/m^2 could be attained simultaneaously, EHD propulsion might be practically useful. In practice, low-speed propulsion systems for long-duration near-space platforms could be perfected. They would use solar power and photovoltaic energy conversion to produce electricity needed to supply the corona-based thrusters. In our work on EHD propulsion, a set of three equations has been established to summarize the thruster performances (see [4] for more details):

$$I = C \times V(V - V_0) \tag{1}$$

$$T = F_{EHD} - F_D = \frac{I \times d}{\mu} - F_D \tag{2}$$

$$\theta \approx \sqrt{C} \times \left(\frac{d}{\mu}\right)^{3/2} \times \frac{1}{\sqrt{F_{EHD}}} \tag{3}$$

with I the discharge current (A/m), V_0 the onset voltage (V), C a constant depending on the electrode geometry and gas properties, T the produced thrust (N/m), F_{EHD} the electro-hydrodynamic force, F_D the drag force due to the electric wind flowing around the collecting cylinder electrode, d the electrode gap (m), μ the ion mobility and θ the electromechanical effectiveness (N/W). Equation (1) was well-known for a long time. Equation (2) highlights that F_{EHD} increases with the current I and the gap d and that a way to increase the thrust T is to reduce the drag F_D. Unfortunately, equation (3) shows that the electromechanical effectiveness decreases when F_{EHD} increases. Moreover, since drag F_D

$\propto v^2$ (with v the electric wind velocity) and $v \propto \sqrt{I}$, equation (2) can be expressed as follows:

$$T = \left(\frac{d}{\mu} - \alpha \right) \times I \qquad (4)$$

where α is a constant. Equation (4) shows that thrust is theoretically proportional to the discharge current.

For instance, in the case of a simple wire-to-cylinder design, Figure 21 shows the discharge current per unit length in span wise (discharge current divided by the electrode span wise, in µA per meter) versus applied voltage in kV, for negative and positive coronas. As it is well-known, one can observe that theoretical curves coming from Equation (1) correctly interpolate the experimental current measurements. Figure 22 presents the measured thrust T per unit span wise length (in mN/m) as a function of the discharge current I (T-I characteristic). It highlights that the measured thrust is proportional to the discharge current, as predicted by equation (4). Moreover, one can say that the corona discharge induces a similar thrust value whatever the sign of the applied high voltage, the difference being smaller than 0.5%. Finally, Figure 23 present the thrust effectiveness θ as a function of the produced thrust. It shows that θ decreases when the produced thrust increases, as theoretically explained by equation (3).

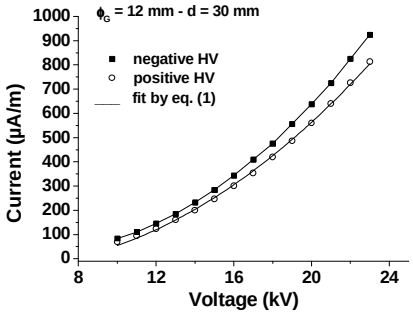

Fig. 21. I-V characteristic: discharge current (per unit length) versus applied voltage.

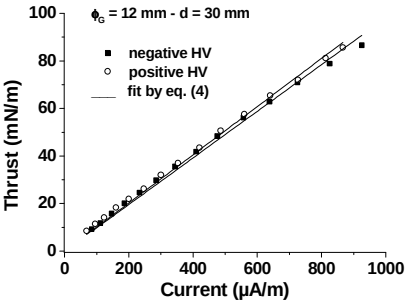

Fig. 22. Thrust versus current (T-I characteristic).

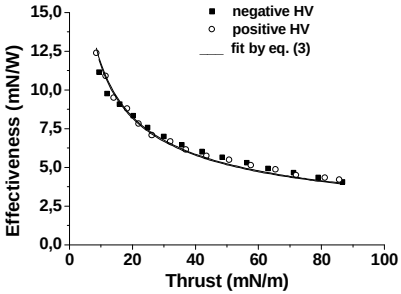

Fig. 23. Effectiveness versus versus thrust (θ-T characteristic).

IV. Conclusion

In this paper, the last results on plasma actuators and their use for airflow separation control have been presented. In a second part, future prospects offered by new plasma actuators such as µ-plasma grid for turbulence manipulation and recent experiments on DC corona discharges used for EFD propulsion have been briefly discussed.

During the oral invited lecture, others applications will be presented.

References

[1] Benard N., Moreau E. (2014). “Electrical and mechanical characteristics of surface AC dielectric barrier discharge plasma actuators applied to airflow control”, Experiments in Fluids (55).

[2] Benard N., Zouzou Z., Claverie A., Sotton J., Moreau E. (2012). “Optical visualization and electrical characterization of fast-rising pulsed DBD for airflow control applications', Journal of Applied Physics (111).

[3] Benard N., Mizuno A., and Moreau E., ‘Manipulation of a grid-generated mixing with an active honeycomb dielectric barrier plasma discharge’, Applied Physics Letters, vol. 107(24), 5 pages, 2015

[4] Moreau E, Benard N, Lan-Sun-Luk JD, Chabriat JP 2013 Electrohydrodynamic force produced by a wire-to-cylinder dc corona discharge in air at atmospheric pressure, Phys D: Applied Physics, Vol 46 (14 pages).

[5] E. Moreau, N. Benard, F. Alicalapa, A. Douyère, “Electrohydrodynamic force produced by a corona discharge between a wire active electrode and several cylinder electrodes – Application to electric propulsion”, Journal of Electrostatics, Vol. 76, pp. 194-200, 2015.

[6] G. O. Christenson E A and Moller P S 1967 Ion-neutral propulsion in atmosspheric media AIAA J. 5 1768–73

[7] Wilson J, Perkins HD, Thompson WK 2009 An investigation of ionic wind propulsion NASA Report NASA/TM 2009-215822.